AIAA JOURNAL
Vol. 52, No. 1, January 2014

Technical Notes

Approximate Aerodynamic and Aeroelastic Modeling of Flapping Wings in Forward Flight

Abhijit Gogulapati*
Ohio State University, Columbus, Ohio 43210
and
Peretz P. Friedmann†
University of Michigan, Ann Arbor, Michigan 48109

DOI: 10.2514/1.J052596

Nomenclature

a	=	distance between pitch axis of airfoil and midchord
C_D, C_L, C_T	=	drag, lift, and thrust coefficients
c	=	airfoil chord
c_r	=	root chord
D	=	drag
$\mathrm{d}\Gamma_{\mathrm{wk}}$	=	circulation of a discrete vortex
F_h, F_v	=	components of aerodynamic force in the horizontal and vertical directions
f	=	flapping frequency
h	=	plunge degree of freedom
i, j, k	=	indices
L	=	lift
L_C	=	circumference of the airfoil
l	=	lead lag degree of freedom
l_0	=	lead lag amplitude
N_θ	=	discretization of the circle
N_{sections}	=	number of wing sections
n_{wksubit}	=	number of wake subiterations
p	=	local static pressure on the airfoil
p_∞	=	freestream pressure
$\mathbf{q}$	=	complex velocity
$\mathcal{R}$	=	real part
Re	=	Reynolds number
R_0	=	radius of the circle in the complex plane
R_j	=	radial location of jth wing section
R_{span}	=	wing span
r_c	=	vortex core radius
r_v	=	distance between vortex and point at which induced velocity is computed
s	=	arc coordinate
s_0	=	origin of the curve that is used to integrate along the airfoil
$s_{\mathrm{wk1}}, s_{\mathrm{wk2}}$	=	arc coordinates of the wakes shed from the trailing and leading edges of the airfoil
T	=	thrust
t	=	time
t_v	=	age of a vortex
$\boldsymbol{U}_I$	=	freestream velocity vector in the $\xi^I - \eta^I$ coordinate system
$\boldsymbol{U}_\infty$	=	freestream velocity vector in the X_{SP}, Y_{SP}, Z_{SP}coordinate system
U_∞	=	magnitude of $\boldsymbol{U}_\infty$
U_I	=	magnitude of $\boldsymbol{U}_I$
U_{ref}	=	reference speed
U_{tip}	=	maximum tip speed
u_∞, v_∞	=	components of the freestream velocity resolved parallel and normal to the stroke plane
u_I, v_I	=	components of $\boldsymbol{U}_I$ resolved in the $\xi^I - \eta^I$ coordinate system
v_{ind}	=	velocity induced by a vortex
$(X_{\mathrm{SP}}, Y_{\mathrm{SP}}, Z_{\mathrm{SP}})$	=	coordinate system fixed to the stroke plane
z_{wk}	=	coordinate of a shed vortex on the complex plane
α	=	pitch angle
α_0	=	pitch amplitude
α_{fs}	=	angle between freestream velocity and the ξ^I axis
β	=	flap angle
β_0	=	flap amplitude
β_{sp}	=	angle between the stroke plane and the freestream velocity vector
Γ_{fs}	=	circulation due to instantaneous pitch angle and freestream
γ_b	=	bound vorticity
γ_{fs}	=	component of vorticity due to instantaneous pitch angle and freestream
$\gamma_{\mathrm{wk1}}, \gamma_{\mathrm{wk2}}$	=	vorticity shed from the trailing and leading edges of the airfoil
ζ	=	complex coordinate in an airfoil coordinate system (superscript identifies the coordinate system)
θ	=	angular coordinate on the circle in the complex plane
μ	=	advance ratio
v_∞	=	kinematic viscosity of the fluid
ξ, η	=	coordinates in an airfoil fixed frame (superscript identifies coordinate system)
π	=	3.14259
ρ_∞	=	freestream density of the fluid
$\tilde{\varphi}$	=	angular position of a vortex or wing section on the stroke plane
φ	=	angular position of a vortex in an airfoil coordinate system
φ_α	=	phase angle
ϕ	=	velocity potential
φ_b	=	velocity potential due to bound vorticity
φ_{wk1}	=	velocity potential due to wake shed from trailing edge
$\lvert\cdot\rvert$	=	absolute value or magnitude
$(\cdot)\lvert_{\mathrm{invis}}$	=	inviscid quantity
$(\cdot)\lvert_{\mathrm{vis}}$	=	viscous quantity
$(\cdot)^*$	=	complex conjugate

Presented as Paper 2011-2008 at the 52nd AIAA/ASME/ASCE/AHS/ASC Structures, Structural Dynamics, and Materials Conference, Denver, CO, 4–7 April 2011; received 1 February 2013; revision received 19 June 2013; accepted for publication 1 July 2013; published online 24 December 2013.

*Postdoctoral Research Fellow, Mechanical and Aerospace Department. Member AIAA.

†François-Xavier Bagnoud Professor, Department of Aerospace Engineering. Fellow AIAA.

I. Introduction

HOVER-CAPABLE flapping-wing micro air vehicles (MAVs), inspired by biological flyers such as insects and hummingbirds,

are suitable for missions involving closed spaces, such as buildings, low altitudes, and over short ranges [1]. The performance of these vehicles in low-speed forward flight conditions is an important practical consideration in the development of realistic configurations. However, this aspect has received considerably less attention compared to the case of hover and motivates the work presented in this note. Here, "low-speed" implies that the ratio of forward speed of the vehicle to the maximum wing-tip velocity (also referred to as the advance ratio) is less than 0.25.

Wake-visualization studies and force measurements on free-flying insects [2,3] suggest that the unsteady force-generating aerodynamic mechanisms that are important in hover [4,5], which include leading-edge vortices (LEVs), wake capture, and tip vortices, are important also in low-speed forward flight. However, their contribution to the aerodynamic force generated by the wings is expected to decrease with increasing forward flight speed. Also, the unsteady mechanisms dissipate faster at lower Re than at higher Re, implying that the impact of fluid viscosity on the aerodynamic loads is likely to increase with decrease of Re.

The impact of wing flexibility on the forward flight performance of flapping wings was examined in [6–8]. Membrane wings reinforced by a metal frame operating at $Re = 20,000$ to $Re = 80,000$ and advance ratios ranging from 0.3 to 8 were considered in [6]. Measurements showed that increasing chordwise flexibility improved the lift-to-drag ratio in high-speed forward flight, whereas spanwise flexibility had a greater impact at lower advance ratios. Membrane wings actuated by combined flap and torsion, at $Re = 1000$ and advance ratio of 0.5, were simulated by combining a linear elastic membrane solver with an unsteady large-eddy simulation code [7]. Aeroelastic calculations, in which effect of inertia forces were neglected, indicated that the flexible wings produced greater lift and thrust compared to rigid wings due to a prolonged attachment of LEVs on the wing surface. In [8], rigid and flexible wings in forward flight (advance ratios of 0.5 to 4) were simulated by combining commercially available structural (FEMSTRESS) and fluid (CFD-ACE+) solvers. A stiffer outboard region enhanced lift, whereas a more flexible inboard region enhanced thrust. To the authors' knowledge, trend studies that examine the effect of wing flexibility on the forces generated by flapping wings in low-speed forward flight have not been considered in literature.

Numerical approaches that offer the best accuracy in aeroelastic analyses involve coupling computational fluid dynamics (CFD) models based on the Navier–Stokes (NS) equations with structural models based on nonlinear finite-element (FE) formulations [5]. However, the computational expense of CFD simulations makes their use impractical in studies focusing on parametric trends, design, and control. Approximate unsteady aerodynamic formulations, which offer a compromise between accuracy and computational expense, are better suited for this purpose.

The development and validation of a nonlinear approximate aeroelastic model suitable for predicting the behavior of flexible flapping wings in hover is described in a previous work by the authors [9]. The aeroelastic model is obtained by coupling a nonlinear FE model of the wing based on MSC MARC® with a nonlinear approximate unsteady aerodynamic model that incorporates LEVs and a wake model. The aerodynamic formulation employed in [9] was modified to incorporate the effects of forward flight speed and fluid viscosity. The modified model, also described in [10], retains several aspects of the hover formulation. Therefore, the current note serves as an extension to [9] and provides concise descriptions of the modifications to the formulation, verification studies conducted using rigid airfoils and wings, and trend studies using anisotropic configurations.

II. Modifications to the Approximate Aerodynamic Model

The unsteady aerodynamic model was originally developed for rigid wings in hover [11,12] and was subsequently modified to incorporate wing flexibility [9]. The formulation is based on two-dimensional potential flow and is applied on the wing in a strip theory manner. The modifications to incorporate effects of forward flight and fluid viscosity are presented in this section. Additional details are available in [9,10].

In the hover model [9,11], a cylinder that is normal to the stroke plane (SP), depicted in Fig. 1a, is used to approximate the airfoil motion and shed wake geometry. Several coordinate systems defined on the normal cylinder (NC), retained from the hover formulation, are employed to incorporate the modifications. The $X_{SP}Y_{SP}Z_{SP}$ coordinate system is shown in Fig. 1a, where the X_{SP}-Y_{SP} plane defines the SP and Z_{SP} is normal to the SP. The (ξ^I, η^I) coordinate system, shown in Figs. 1a and 1b, is fixed to the NC with ξ^I parallel to the SP and η^I parallel to Z_{SP}, indicated using the superscript I. The origin of the (ξ^{fa}, η^{fa}) coordinate system is fixed at the center of rotation of the airfoil (i.e., the intersection of the feathering axis of the wing and the NC), and ξ^{fa} is parallel to the zero lift line of the airfoil (Fig. 1b). Each airfoil has three degrees of freedom defined in (ξ^I, η^I), shown in Fig. 1b: lead–lag l, plunge h, and pitch α, which are defined as positive along the ξ^I, η^I axes and clockwise, respectively.

A. Extension to Forward Flight

Experimental observations on biological flyers [13,14] suggest that a transition from hover to forward flight involves tilting the SP. Therefore, it is assumed in the current study that the wake surface for wings in forward flight is cylindrical and tilted with respect to the freestream velocity so that it is normal to the SP, as depicted in Fig. 2. With these assumptions, the NC that was used for hover is also used as the airfoil–wake surface in forward flight.

The freestream velocity vector due to forward flight, assumed to lie in the Y_{SP}-Z_{SP} plane, is described using two components u_∞ and v_∞, depicted in Fig. 1a. The components are determined using Eq. (1):

$$u_\infty = -\mu U_{\text{tip}} \quad \text{and} \quad v_\infty = u_\infty \tan(\beta_{\text{sp}}) \tag{1}$$

where β_{SP} is shown in Figs. 1a and 2, and the definition of advance ratio is inspired from the definition employed in rotary-wing studies [15]. The components u_∞ and v_∞ are negative due to the sign convention adopted to describe the freestream velocity; see Fig. 2. Therefore, the negative sign in Eq. (1) ensures that μ, which is defined as positive, yields negative values of u_∞ and v_∞.

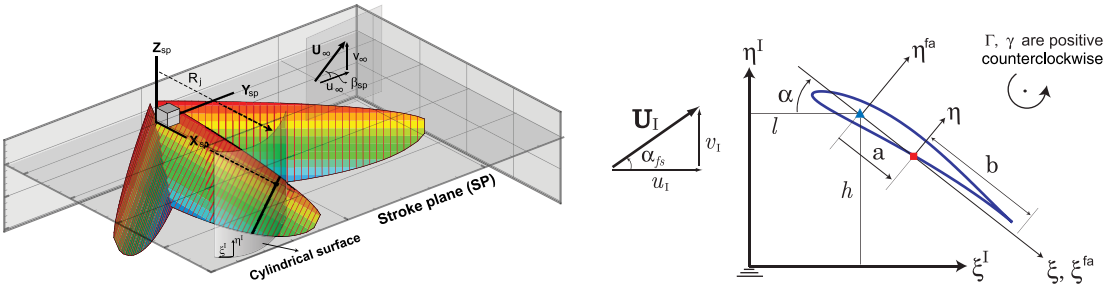

a) Stroke plane and cylindrical surface

b) Airfoil degrees of freedom and coordinate systems used

Fig. 1 Stroke plane, cylindrical surface, and coordinate systems employed in the hover formulation [9].

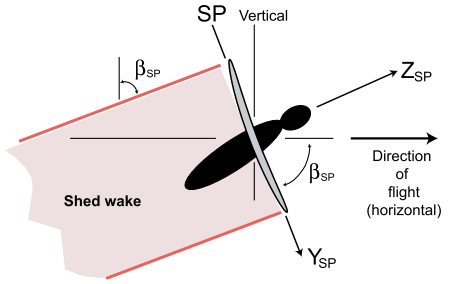

Fig. 2 Tilting of the stroke plane and wake surface in forward flight.

The extension to forward flight is achieved by incorporating the components of freestream velocity on the straightened NC into the expressions used to calculate quasi-steady vorticity and wake evolution. These components are obtained from u_∞, v_∞, and the instantaneous angular position of the wing section or shed vortex on the SP as follows.

At a wing section:

$$u^I_{w_j} = -u_\infty \cos\tilde{\varphi}_{w_j}, \qquad v^I_{w_j} = v_\infty \tag{2a}$$

At a shed vortex:

$$u^I_{\Gamma_k} = -u_\infty \cos\tilde{\varphi}_{\Gamma_k}, \qquad v^I_{\Gamma_k} = v_\infty \tag{2b}$$

where $\tilde{\varphi}$ is depicted in Fig. 3, and the subscripts w_j and Γ_k denote the jth wing section and kth shed vortex, respectively. The modified expressions are given in Secs. II.C and II.E.

B. Modifications to Include the Effect of Fluid Viscosity in Shed Vorticity

In a viscous fluid, the influence of shed vorticity at a point of interest decays with increase in distance as well as the age of the vortex. In the current study, the decay of vortex strength is incorporated into the expression of induced velocity due to shed vorticity [10] using the relations obtained for a Lamb–Oseen vortex [16], as shown in Eq. (3):

$$\mathrm{d}\Gamma|_{\mathrm{vis}} = \mathrm{d}\Gamma|_{\mathrm{invis}}\left(1 - e^{-\frac{r_v^2}{4\nu_\infty t_v}}\right) \tag{3}$$

The effect of viscosity is incorporated into the formulation by including the exponential decay term on the right-hand side (RHS) of Eq. (3) into the constraint conditions used to determine the shed vorticity, the expressions used to compute wake induced and bound vorticity, wake evolution, and calculation of the pressure from the unsteady Bernoulli equation. These are discussed in Secs. II.D, II.E, and II.F.

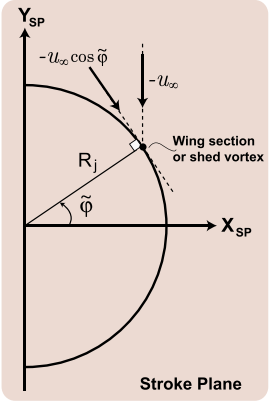

Fig. 3 Component of u_∞ normal to the instantaneous position of the wing section or shed vortex.

C. Calculation of Quasi-Steady Vorticity

The quasi-steady component of vorticity [11] is computed by neglecting the effect of the shed wake. Incorporating the effect of forward flight requires modification of the vorticity and circulation due to the instantaneous pitch angle, denoted by γ_{fs} and Γ_{fs} in [9]. The modified expressions are given by

$$\gamma_{\mathrm{fs}}(\theta, t) = -2U_I[\sin(\theta - \alpha - \alpha_{\mathrm{fs}}) + \sin(\alpha + \alpha_{\mathrm{fs}})]$$

$$\Gamma_{\mathrm{fs}}(t) = -4\pi R_0 U_I \sin(\alpha + \alpha_{\mathrm{fs}})$$

where, $U_I = \sqrt{(u_\infty \cos\tilde{\varphi}_w)^2 + v_\infty^2}$ and $\alpha_{\mathrm{fs}} = \tan^{-1}(-\frac{v_\infty}{u_\infty \cos\tilde{\varphi}_w})$ is shown in Fig. 1b.

D. Calculation of Shed Vorticity

The modified expression of induced velocity on the circle due to a shed wake vortex, given in Eq. (4), is obtained by incorporating Eq. (3) into the expression of induced velocity due to an inviscid vortex from [11]:

$$v_{\mathrm{ind}}(\theta, t)|_{\mathrm{vis}} = -\frac{1}{2\pi R_0}\oint_{\mathrm{wk}}\left[\mathcal{R}\left(\frac{z_{\mathrm{wk}} + R_0 e^{i\theta}}{z_{\mathrm{wk}} - R_0 e^{i\theta}}\right) \times \mathrm{d}\Gamma_{\mathrm{wk}}\left(1 - e^{-\frac{r_v^2}{4\nu_\infty t_v}}\right)\right] \tag{4}$$

where $r_v = |z_{\mathrm{wk}} - R_0 e^{i\theta}|$. The RHS of Eq. (4) is incorporated into Eqs. (22, 23, 24) in [9], which represent the stagnation condition at the leading edge (LE), the Kutta condition at the trailing edge, and the wake-induced vorticity on the circle in the complex plane.

E. Wake Evolution

Vortices on the straightened NC are convected using the Rott–Birkhoff equation [16], which yields the induced velocity at any point due to the bound and shed vorticity and freestream velocity in the airfoil–wake system. The modified expression of induced velocity is obtained by incorporating Eqs. (2) and (3) into Eq. (35) in [9]:

$$\mathbf{q}^*(\zeta^I)|_{\mathrm{vis}} \asymp \sum_{k=1}^{\infty}\left[-(u_\infty \cos\tilde{\varphi}_{\Gamma_k} + iv_\infty) + \frac{(\zeta^I - \zeta_k^I)^*}{2\pi i(r_c^2 + |\zeta^I - \zeta_k^I|^2)}\mathrm{d}\Gamma_k\left(1 - e^{-\frac{r_{v_k}^2}{4\nu_\infty t_{v_k}}}\right)\right]$$

where $i = \sqrt{-1}$, $r_{v_k} = |\zeta^I - \zeta_k^I|$, and the subscript k denotes the kth vortex.

F. Calculation of Aerodynamic Loads Using the Unsteady Bernoulli Equation

The unsteady Bernoulli equation, derived in the stationary $\xi^{fa} - \eta^{fa}$ coordinate system [9], is

$$\frac{p_\infty - p}{\rho_\infty} = \frac{\partial\phi}{\partial t} + \frac{1}{2}\left[\left(\frac{\partial\phi}{\partial\xi^{fa}}\right)^2 + \left(\frac{\partial\phi}{\partial\eta^{fa}}\right)^2\right] - \left(v_\xi^{fa}\frac{\partial\phi}{\partial\xi^{fa}} + v_\eta^{fa}\frac{\partial\phi}{\partial\eta^{fa}}\right)$$

where $\phi(s, t) = \phi_b(s, t) + \phi_{\mathrm{wk1}}(s, t)$. The expressions of ϕ_b and ϕ_{wk1} for inviscid flow are given in [9]. Incorporating the effect of viscosity, the modified expressions are as follows.

For $0 < s < s_{\mathrm{wk2}}$,

$$\phi_b(s, t) = \phi_0 + \int_0^s \gamma_b\,\mathrm{d}s$$

For $s_{\mathrm{wk2}} < s < L_C$,

$$\phi_b(s,t) = \phi_0 + \int_0^{s_{\text{wk2}}-} \gamma_b \, \mathrm{d}s + \int_{s_{\text{wk2}}+}^{s} \gamma_b \, \mathrm{d}s + \int_{L_{\text{wk2}}} \{\gamma_{\text{wk2}}(\varsigma,t)(1 - e^{-\frac{r_v^2}{4\nu_\infty r_v}})\} \, \mathrm{d}\varsigma \quad (5)$$

The modified expression for ϕ_{wk1} is given by

$$\phi_{\text{wk1}}(s,t) = \int_{L_{\text{wk1}}} \left\{ \frac{\gamma_{\text{wk1}}(\varsigma,t)}{2\pi} \varphi(\varsigma,s,t)(1 - e^{-\frac{r_v^2}{4\nu_\infty r_v}}) \right\} \mathrm{d}\varsigma \quad (6)$$

where $\varphi(\varsigma,s,t) = \text{argument}(\zeta^{fa}_{\text{wk1}}(\varsigma,t) - \zeta^{fa}(s))$. In Eqs. (5) and (6), $r_v = |\zeta^{fa}_{\text{wk1}}(\varsigma,t) - \zeta^{fa}(s)|$, and ς is a dummy variable used in the integration.

III. Results and Discussion

Three sets of results are presented: 1) aerodynamic comparisons for rigid airfoils, 2) aerodynamic comparisons for rigid wings in forward flight, and 3) aeroelastic studies on anisotropic wings in forward flight. Additional information can be found in [10,17]. The emphasis of the results provided in this section is on rigid and flexible wings in forward flight. However, a brief discussion on airfoils undergoing prescribed motion is included because they correspond to cases wherein the impact of fluid viscosity is noticeable.

The approximate results were obtained using the modified formulation assuming leading-edge separation. The transient aerodynamic loads are calculated using the unsteady Bernoulli equation. In previous studies [9], the authors found that the airfoil–wake interaction generated large-amplitude numerical oscillations, or "spikes", in the aerodynamic loads. These oscillations had to be eliminated before applying the unsteady loads on the flexible structure in aeroelastic simulations. The oscillations are not critical to simulations involving rigid airfoils and wings. However, smoothing the signals improves clarity when comparing the time histories of the aerodynamic loads with CFD results. The load signals obtained from the approximate aerodynamic model for rigid cases (and the aeroelastic model for flexible cases) are postprocessed using zero-phase digital filters available in MATLAB® (version 8.0) using the *filtfilt* command.

A. Aerodynamic Comparisons

Results are presented for flat plate airfoils undergoing prescribed motion and rigid Zimmerman wings in forward flight.

1. Airfoil Cases

The forces generated by airfoils undergoing prescribed motion for the case of hover and forward flight are presented in Fig. 4. The lift and drag are components of the aerodynamic force parallel to the η^I and ξ^I axes, respectively. The airfoil kinematics are described by Eq. (7), where the pitching is about the midchord:

$$l(t) = l_0 \sin(2\pi f t) \quad \text{and} \quad \alpha(t) = \frac{\pi}{2} + \alpha_0 \sin(2\pi f t + \varphi_\alpha)$$

The nondimensional forces are defined as follows:

$$C_L = \frac{L}{(1/2)\rho_\infty U_{\text{ref}}^2 c} \quad \text{and} \quad C_D = \frac{D}{(1/2)\rho_\infty U_{\text{ref}}^2 c}$$

The results are obtained for $Re = 100$, $l_0 = c = 1$ m, $U_{\text{ref}} = 1.0$ m/s, $f = 1/2\pi$ Hz, $\alpha_0 = \pi/4$ rad, and $\phi_\alpha = \pi/3$ rad for a hypothetical fluid that has $\rho_\infty = 1$ kg/m^3 and $\nu_\infty = 0.01$ m^2/s. The CFD-based results are taken from [18]. The approximate results were obtained for $N_\theta = 200$, $r_c = 0.1c$, and $n_{\text{wksubmit}} = 4$. A circulation limit [17] was fixed at 2.0 to prevent the shedding of unrealistic vortices in the system.

The force coefficients obtained for hover by assuming inviscid flow and incorporating viscous effects are shown in Fig. 4a. Simulations using the approximate model were conducted using 500 time steps per cycle. The comparisons illustrate that incorporating the effect of viscosity improves correlation with CFD based results. In particular, the improvement is noticeable for C_D. These results suggest that the influence of fluid viscosity in the interactions involving shed vorticity is important for this case. The forces generated by the airfoil in the presence of a freestream is shown in Fig. 4b. The freestream velocity vector is parallel to the ξ^I axis and has a magnitude equal to $0.2U_{\text{ref}}$. Simulations with the approximate model were carried out by including effect of viscosity. Comparisons indicate that the approximate model produces acceptable agreement with CFD. In the approximate results presented in Fig. 4, a significant number of the numerical spikes were eliminated by the use of filters during postprocessing; however, some spikes could not be eliminated and are noticeable, particularly in cycles 3 to 5.

2. Rigid Wings in Forward Flight

The results for the rigid wings are based on a Zimmerman planform with $R_{\text{span}} = 75$ mm and $c_r = 25$ mm [19]. The CFD simulations were conducted using the numerical framework that solves the finite-volume-based NS equations for laminar, incompressible flow using a pressure-based algorithm [20,21]. The aerodynamic loads obtained using the approximate aerodynamic model were computed for the following set of parameters: $N_{\text{sections}} = 59$, $N_\theta = 100$, $r_c = 0.05 \times$ chord, and $n_{\text{wksubit}} = 4$. The simulations were conducted for air $\rho_\infty = 1.209$ kg/m^3, $\nu_\infty = 1.568 \times 10^{-5}$ m^2/s). At the start of the motion, the wing lies in the X_{SP}-Z_{SP} plane, and the flapping axis coincides with Z_{SP}. The lift and thrust generated by the wings are the components of the aerodynamic force resolved along Y_{SP} and Z_{SP}, shown in Fig. 1a, respectively. The corresponding nondimensional quantities are defined in Eq. (7):

$$C_L = \frac{L}{(1/2)\rho_\infty U_{\text{ref}}^2 R_{\text{span}} c_r} \quad \text{and} \quad C_T = \frac{T}{(1/2)\rho_\infty U_{\text{ref}}^2 R_{\text{span}} c_r} \quad (7)$$

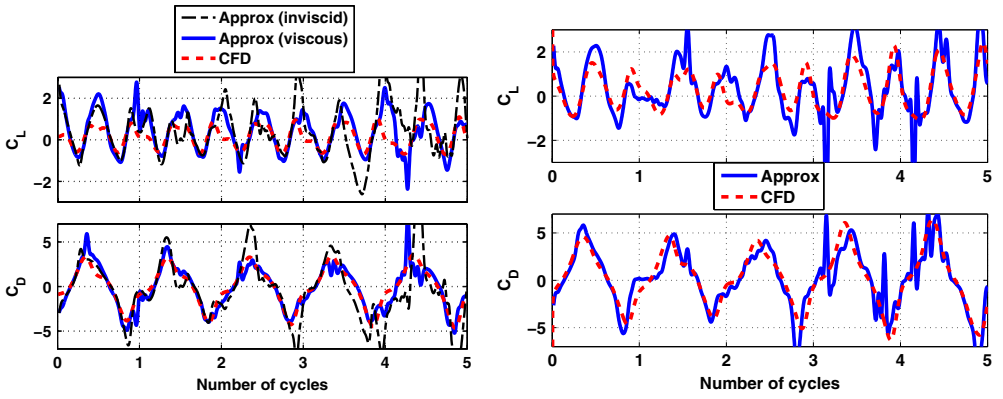

a) Force coefficients for case of hover

b) Force coefficients for case with freestream

Fig. 4 Force coefficients for airfoils undergoing prescribed motion.

Table 1 Errors in peak-to-peak and mean lift predictions

Advance ratio	Stroke plane inclination, deg	Percent error in peak-to-peak lift, %	Percent error in mean lift, %
0.0	0	50	1.2
0.05	14	34.6	0.46
0.10	21.2	26.6	1.73
0.15	27.7	15.6	0.18
0.20	34	10.2	4.2
0.25	40	19.5	13.8

where $U_{\text{ref}} = 4f\beta_0 R_{\text{span}}$, following the definition used in [22]. The flapping motion, prescribed about Z_{SP}, is described by $\beta(t) = \beta_0 \sin(2\pi f t)$, and the Reynolds number, based on the reference speed and root chord, is given by

$$Re = \frac{U_{\text{ref}} c_r}{\nu_\infty} \tag{8}$$

The forces generated by the wings in forward flight are obtained for combinations of μ and β_{sp} that are based on experimentally obtained data for hawkmoths in forward flight [13]. The specific combinations used in the current study are listed in Table 1. The components of freestream velocity are calculated using Eq. (1), where $U_{\text{tip}} = 2\pi\beta_0 f R_{\text{span}}$.

Comparisons of time histories for the case of $\mu = 0.25$ are shown in Fig. 5a. The mean, or time-averaged, lift coefficients generated by rigid wings for $\beta_0 = 35$ deg, $f = 10$ Hz, and various advance ratios, are shown in Fig. 5b. The CFD and approximate simulations were conducted by using 500 and 300 time steps per flapping cycle, respectively. In the absence of wing pitch, the thrust generated by thin rigid wings is several orders of magnitude lower than lift [9]; therefore, results for this quantity are not presented. The simulation times for the CFD-based and approximate results were six days using 24 2.53 GHz Intel Xeon E5540 processors (3 GB of RAM per processor) and two days using a single 3.06 GHz Intel Xeon processor (2 GB of RAM), respectively.

The errors in peak-to-peak and mean lift coefficients at various advance ratios are provided in Table 1. The error is defined as the difference in the quantities predicted by the two approaches normalized using the peak-to-peak lift obtained from the CFD simulations, averaged over cycles 2 through 5. The larger discrepancies in peak-to-peak lift at lower advance ratios are attributed to differences in wake structures. Effects of spanwise flow and tip vortices may be also be important for the combination of amplitude and flapping frequency considered. These aspects are not captured by the approximate aerodynamic model. The wake shed during previous cycles is carried away from the wing more rapidly as the freestream velocity increases. Therefore, the discrepancy in unsteady loads due to the wake structures decreases with increase in advance ratio. This also implies that the impact of spanwise flow, tip vortices, and three-dimensional wake effects on the unsteady loads reduces with increase in advance ratio.

Increasing the forward flight speed was found to increase the magnitude of peak force generated during the first half of the flapping cycle (advancing wing) and reduce the magnitude the peak force generate during the second half of the flapping cycle (retreating wing); see Fig. 5a. This trend is also reflected in Fig. 5b, which shows that the mean lift coefficient decreases (becomes more negative) with increasing forward flight speed. The approximate model captures the trend accurately. The errors in mean lift coefficient, normalized using the peak-to-peak lift obtained from the CFD simulations, are listed in Table 1. These errors indicate that the mean lift predicted by the approximate model has acceptable accuracy (i.e., error $\leq$20%). The comparisons presented demonstrate that the modified aerodynamic model is suitable for trend-type studies for wings in forward flight.

The lift coefficients generated by rigid wings undergoing flap and combined flap-pitch motions for several combinations of flapping frequencies, amplitudes, and advance ratios were computed. The Reynolds numbers for the various cases were between 416 and 11,687. For fixed values of stroke amplitudes and advance ratio, the values of C_L computed at various flapping frequencies are very similar. Sample results for $\beta_0 = 20$ deg, $\mu = 0.25$, at $f = 2.5$ and 10 Hz are shown in Fig. 6, where CFD and approximate results are shown separately. Based on the definitions of C_L and Re, given in Eqs. (7) and (8), the trends obtained indicate that C_L is insensitive to Re for the range of values considered and that the lift is proportional to f^2.

B. Aeroelastic Results

Aeroelastic simulations were conducted using anisotropic Zimmerman wings that are built from an unstressed CAPRAN film (membrane) supported by a carbon-fiber-based spar-batten skeleton [19]. Following the notation used in [19], the wings are labeled as LiB1, where $i = 1, 2, 3$ denotes the number of prepreg layers in the LE spar. Structural dynamic modeling of the anisotropic wings in MARC, including determination of material properties, is described in [9]. The equations of motion obtained using the updated Lagrangian method are integrated forward in time using a single-step

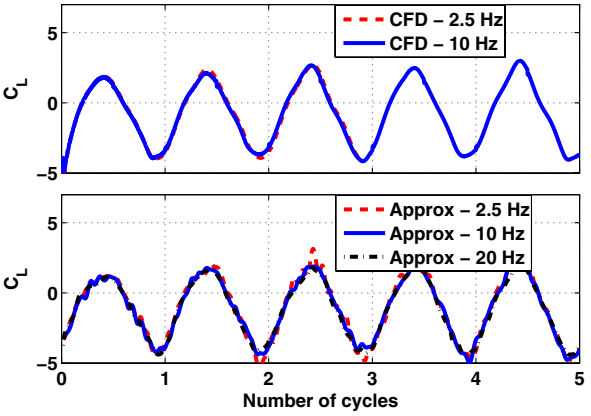

Fig. 6 Lift coefficients generated by rigid wings for $\beta_0 = 20$ deg, $\mu = 0.25$.

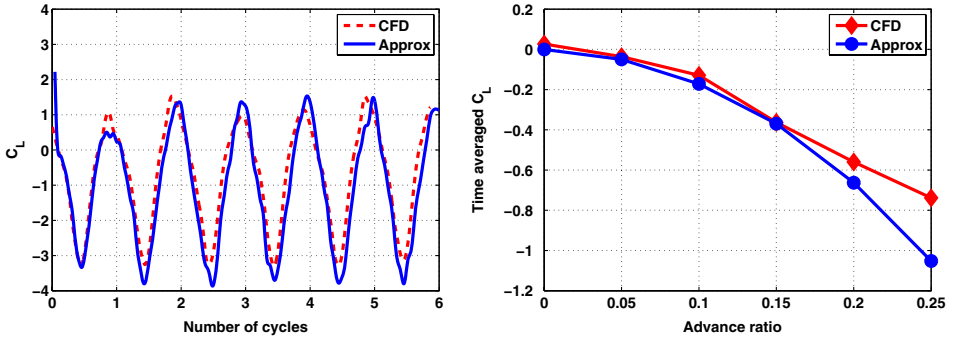

a) $\mu = 0.25$ **b) Mean lift for a range of advance ratios**

Fig. 5 Force coefficients generated by rigid wings in forward flight: $\beta_0 = 35$ deg, $f = 10$ Hz.

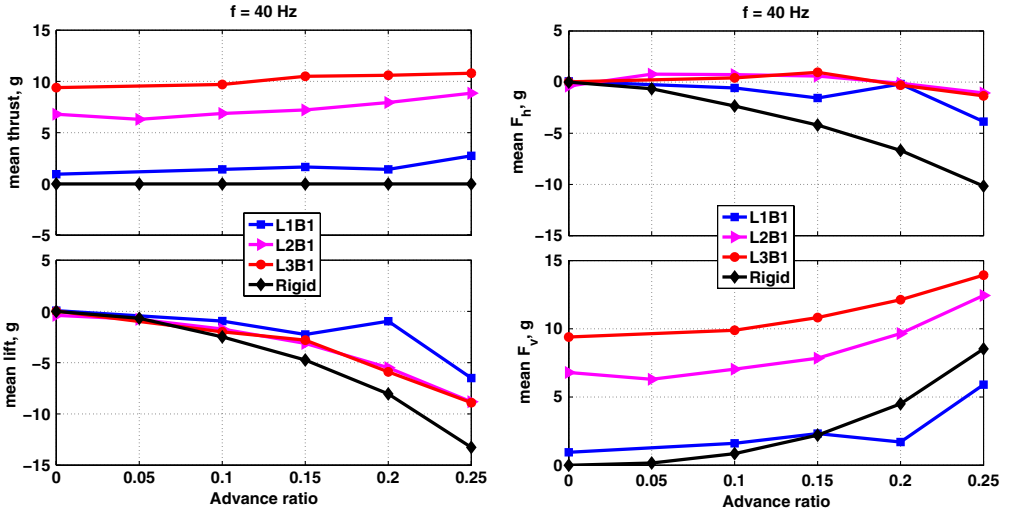

a) Mean lift and thrust **b) Mean horizontal and vertical forces**

Fig. 7 Mean forces, in grams, generated by rigid and flexible wings at $f = 40$ Hz.

Houbolt numerical scheme [23]. During the simulations, a pressure-based filter [17] described by Eq. (9) was used to limit the magnitude of numerical noise that is transmitted to the flexible wing:

$$p_{\text{app}} = \frac{p_{\text{comp}}}{|p_{\text{comp}}|}\min\{|p_{\text{comp}}|, |p_{\text{limit}}|\} \tag{9}$$

where p_{comp}, p_{limit}, and p_{app} are the computed, applied, and limit values (respectively) of aerodynamic pressure. For the cases considered, $p_{\text{limit}} = 36p_{\text{ref}}$, where the reference pressure is given by $p_{\text{ref}} = (1/2)\rho_\infty U_{\text{tip}}^2$ and $U_{\text{tip}} = 2\pi f \beta_0 R_{\text{span}}$ [17].

The mean aerodynamic forces generated by the configurations L1B1, L2B1, L3B1, and a rigid wing, actuated using a sinusoidal flap actuation, for a range of forward flight conditions and flapping frequencies were computed. Sample results, obtained for $\beta_0 = 35$ deg, $f = 40$ Hz, and the forward flight conditions corresponding to the values given in Table 1, are shown in Fig. 7. The magnitude of the freestream velocities were determined based on the tip speed of a rigid wing undergoing the same kinematics. The simulations, conducted for a total of five flapping cycles using 300 time steps per cycle to discretize the motion, indicated that an approximate steady state was achieved after two cycles. Therefore, the mean forces are obtained by time-averaging the transient forces over cycles 2 through 5. The mean forces computed for one wing were multiplied by a factor of 2 so as to approximate the force generated by a vehicle employing a pair of wings.

The mean lift and thrust generated by rigid and flexible wings are shown in Fig. 7a. The results indicate that the lift decreases (becomes more negative) and the thrust increases with increase in forward flight speed. The change in thrust is somewhat small compared to the change in lift. Also, different wings produce maximum mean thrust at different frequencies; L1B1 produces maximum thrust at $f = 10$ Hz (results not presented here), whereas L3B1 produces the maximum thrust at $f = 40$ Hz (see Fig. 7a). Similar trends were observed for the case of hover [9].

The mean horizontal and vertical forces generated by the wings, denoted by F_h and F_v, respectively, that indicate the propulsive and payload capacity of the wings are shown in Fig. 7b. The horizontal and vertical directions are shown in Fig. 2. Note that both F_h and F_v are positive in an actual vehicle, and a negative value of F_h denotes drag. The results show that F_v increases and F_h decreases with increase in forward flight speed, and wing flexibility has a beneficial influence. The flexible configurations have higher payload capacity and lower drag compared to rigid wings. Configurations L1B1 and L3B1 have the largest payload capacity and least drag at 10 and 40 Hz, respectively. These results indicate that the trends in force generation obtained for wings in hover also apply to forward flight.

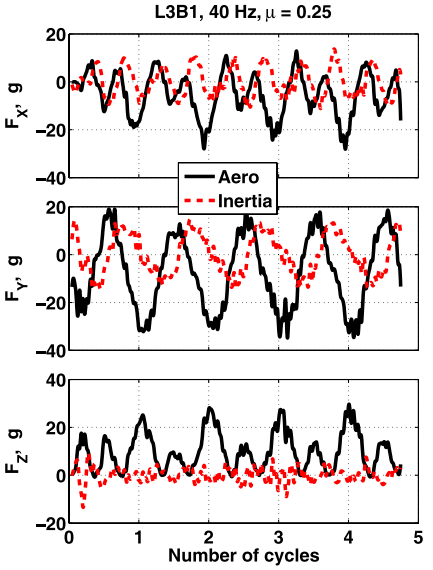

Fig. 8 Aerodynamic and inertia loads acting on L3B1: $\beta_0 = 35$ deg, $\mu = 0.25$, and $f = 40$ Hz.

The aerodynamic and inertia loads acting on the anisotropic configurations were calculated for a range of flapping frequencies and advance ratios using Eq. (44) in [9]. Results obtained for configuration L3B1, $\mu = 0.25$, and $f = 40$ Hz are shown in Fig. 8. These results, and similar results not presented here, indicate that the aerodynamic and inertia loads are comparable in magnitude. Similar trends were obtained for the case of hover [9].

IV. Conclusions

An approximate aerodynamic model for flapping wings, originally developed for hover, was extended to forward flight. The effect of viscosity, modeled as a decay of shed vorticity, was also incorporated into the calculation of induced velocity. The following conclusions can be gleaned from the results obtained for rigid airfoils, rigid wings, and anisotropic wings.

1) The forces generated by airfoils undergoing prescribed motions at low Reynolds number ($Re = 100$) show that incorporating the effect of viscosity in the approximate aerodynamic model improved correlation with CFD-based results.

2) The transient as well as time-averaged forces computed using the modified approximate aerodynamic model show acceptable agreement with CFD results for rigid Zimmerman wings in forward

flight. The trends are also captured in an accurate manner. Thus, the modified approximate aerodynamic model is a useful tool for conducting trend-type studies on flapping-wing MAVs in hover and forward flight.

3) The forces generated by rigid wings for a given kinematic pattern are insensitive to Reynolds numbers and scale with the square of the flapping frequency. The range of Reynolds numbers considered in the current study was 416 to 11,687.

4) For the cases considered, flexible wings have larger payload capacity and lower drag when compared to rigid wings in both hover and forward flight. Different flexible configurations perform better at different flapping frequencies, implying that the choice of the "best" flexible configuration depends on the flapping frequency. A similar behavior was also noted in hover.

5) The inertia and aerodynamic loads acting on the anisotropic configurations considered in the current study are comparable in magnitude. The significance of aeroelastic interactions and the relative importance of aerodynamic and inertia loading is configuration-dependent.

Acknowledgments

This work was supported by the U.S. Air Force Office of Scientific Research's Multidisciplinary University Research Initiative with Douglas R. Smith as Program Director. The authors would like to thank W. Shyy for his input as well as P. Trizila and H. Aono for providing the computational-fluid-dynamics-based results for the rigid airfoils and wings.

References

[1] Mueller, T. J., *Fixed and Flapping Wing Aerodynamics for Micro Air Vehicle Applications*, Vol. 195, Progress in Aeronautics and Astronautics, AIAA, Reston, VA, 2001, pp. 6–13, Chap. 1.

[2] Dudley, R., and Ellington, C. P., "Mechanics of Forward Flight in Bumblebees: 2. Quasi-Steady Lift and Power Requirements," *Journal of Experimental Biology*, Vol. 148, No. 1, 1990, pp. 53–88.

[3] Willmott, A. P., Ellington, C. P., and Thomas, A. L. R., "Flow Visualization and Unsteady Aerodynamics in the Flight of the Hawkmoth, Manduca Sexta," *Philosophical Transactions Royal Society of London B*, Vol. 352, No. 1351, 1997, pp. 303–316. doi:10.1098/rstb.1997.0022

[4] Sane, S. P., "The Aerodynamics of Insect Flight," *Journal of Experimental Biology*, Vol. 206, 2003, pp. 4191–4208. doi:10.1242/jeb.00663

[5] Shyy, W., Aono, H., Chimakurthi, S., Trizila, P., Kang, C.-K., Cesnik, C., and Liu, H., "Recent Progress in Flapping Wing Aerodynamics and Aeroelasticity," *Progress in Aerospace Sciences*, Vol. 46, No. 7, 2010, pp. 284–327. doi:10.1016/j.paerosci.2010.01.001

[6] Hu, H., Kumar, A. G., Abate, G., and Albertani, R., "An Experimental Study of Flexible Membrane Wings in Flapping Flight," *46th AIAA Aerospace Sciences Meeting and Exhibit*, AIAA Paper 2009-0876, Jan. 2009.

[7] Gopalakrishnan, P., "Unsteady Aerodynamic and Aeroelastic Analysis of Flapping Flight," Ph.D. Thesis, Dept. of Mechanical Engineering, Virginia Polytechnic Inst. and State Univ., Blacksburg, VA, 2008.

[8] Ho, S., Nassef, H., Pornsinsirirak, N., Tai, Y., and Ho, C., "Unsteady Aerodynamics and Flow Control for Flapping Wing Flyers," *Progress in Aerospace Sciences*, Vol. 39, No. 8, 2003, pp. 635–681. doi:10.1016/j.paerosci.2003.04.001

[9] Gogulapati, A., Friedmann, P. P., Kheng, E., and Shyy, W., "Approximate Aeroelastic Modeling of Flapping Wings in Hover," *AIAA Journal*, Vol. 51, No. 3, 2013, pp. 567–583. doi:10.2514/1.J051801

[10] Gogulapati, A., and Friedmann, P. P., "Approximate Aeroelastic Analysis of Flapping Wings in Hover and Forward Flight," *52nd AIAA/ASME/ASCE/AHS/ASC Structures, Structural Dynamics, and Materials Conference*, AIAA Paper 2011-2008, April 2011.

[11] Ansari, S. A., Żbikowski, R., and Knowles, K., "Non-Linear Unsteady Aerodynamic Model for Insect-Like Flapping Wing in the Hover. Part 1: Methodology and Analysis," *Proceedings of the IMechE Part G Journal of Aerospace Engineering*, Vol. 220, No. 2, 2006, pp. 61–83. doi:10.1243/09544100JAERO49

[12] Ansari, S. A., Żbikowski, R., and Knowles, K., "Non-Linear Unsteady Aerodynamic Model for Insect-Like Flapping Wing in the Hover. Part 2: Implementation and Validation," *Proceedings of the IMechE Part G Journal of Aerospace Engineering*, Vol. 220, No. 2, 2006, pp. 169–186. doi:10.1243/09544100JAERO50

[13] Willmott, A. P., and Ellington, C. P., "The Mechanics of Flight in the Hawkmoth Manduca Sexta: I. Kinematics of Hovering and Forward Flight," *Journal of Experimental Biology*, Vol. 200, 1997, pp. 2705–2722.

[14] Tobalske, B. W., Warrick, D. R., Clark, C. J., Powers, D. R., Hedrick, T. L., Hyder, G. A., and Biewener, A. A., "Three-Dimensional Kinematics of Hummingbird Flight," *Journal of Experimental Biology*, Vol. 210, No. 13, 2007, pp. 2368–2382. doi:10.1242/jeb.005686

[15] Leishman, J. G., *Principles of Helicopter Aerodynamics*, 2nd ed., Cambridge Univ. Press, New York, 2006, Chap. 2.

[16] Saffman, P. G., *Vortex Dynamics*, Cambridge Univ. Press, Cambridge, England, U.K., 1992, Chap. 13.

[17] Gogulapati, A., "Nonlinear Approximate Aeroelastic Analysis of Flapping Wings in Hover and Forward Flight," Ph.D. Thesis, Univ. of Michigan, Ann Arbor, MI, 2011.

[18] Trizila, P., Kang, C. K., Aono, H., Shyy, W., and Visbal, M., "Low-Reynolds-Number Aerodynamics of a Flapping Rigid Flat Plate," *AIAA Journal*, Vol. 49, No. 4, 2011, pp. 806–823. doi:10.2514/1.J050827

[19] Wu, P., Ifju, P., Stanford, B., Sallstrom, E., Ukeiley, L., Love, R., and Lind, R., "A Multidisciplinary Experimental Study of Flapping Wing Aeroelasticity in Thrust Production," *50th AIAA/ASME/ASCE/AHS/ASC Structures, Structural Dynamics, and Materials Conference*, AIAA Paper 2009-2413, May 2009.

[20] Aono, H., Kang, C.-K., Cesnik, C. E. S., and Shyy, W., "A Numerical Framework for Isotropic and Anisotropic Flexible Flapping Wing Aerodynamics and Aeroelasticity," *28th AIAA Applied Aerodynamics Conference*, AIAA Paper 2010-5082, June–July 2010.

[21] Kang, C. K., Aono, H., Cesnik, C. E. S., and Shyy, W., "Effects of Flexibility on the Aerodynamic Performance of Flapping Wings," *Journal of Fluid Mechanics*, Vol. 689, No. 1, 2011, pp. 32–74. doi:10.1017/jfm.2011.428

[22] Aono, H., Chimakurthi, S., Wu, P., Sallstrom, E., Stanford, B., Cesnik, C., Ifju, P., Ukeiley, L., and Shyy, W., "A Computational and Experimental Study of Flexible Flapping Wing Aerodynamics," *48th AIAA Aerospace Sciences Meeting*, AIAA Paper 2010-554, Jan. 2010.

[23] Chung, J., and Hulbert, G. M., "A Family of Single-Step Houbolt Time Integration Algorithms for Structural Dynamics," *Computational Methods in Applied Mechanics and Engineering*, Vol. 118, Nos. 1–2, 1994, pp. 1–11. doi:10.1016/0045-7825(94)00011-5

R. Gordnier
Associate Editor